

Image recombination transform algorithm for superresolution structured illumination microscopy

Xing Zhou
Ming Lei
Dan Dan
Baoli Yao
Yanlong Yang
Jia Qian
Guangde Chen
Piero R. Bianco

Image recombination transform algorithm for superresolution structured illumination microscopy

Xing Zhou,^{a,b} Ming Lei,^{a,*} Dan Dan,^a Baoli Yao,^{a,*} Yanlong Yang,^a Jia Qian,^a Guangde Chen,^b and Piero R. Bianco^c

^aChinese Academy of Sciences, Xi'an Institute of Optics and Precision Mechanics, State Key Laboratory of Transient Optics and Photonics, No. 17 Xinxi Road, Xi'an, Shaanxi 710119, China

^bXi'an Jiaotong University, School of Science, No. 28 Xianning West Road, Xi'an, Shaanxi 710049, China

^cUniversity at Buffalo, Department of Microbiology and Immunology, No. 12 Capen Hall, Buffalo, New York 14214, United States

Abstract. Structured illumination microscopy (SIM) is an attractive choice for fast superresolution imaging. The generation of structured illumination patterns made by interference of laser beams is broadly employed to obtain high modulation depth of patterns, while the polarizations of the laser beams must be elaborately controlled to guarantee the high contrast of interference intensity, which brings a more complex configuration for the polarization control. The emerging pattern projection strategy is much more compact, but the modulation depth of patterns is deteriorated by the optical transfer function of the optical system, especially in high spatial frequency near the diffraction limit. Therefore, the traditional superresolution reconstruction algorithm for interference-based SIM will suffer from many artifacts in the case of projection-based SIM that possesses a low modulation depth. Here, we propose an alternative reconstruction algorithm based on image recombination transform, which provides an alternative solution to address this problem even in a weak modulation depth. We demonstrated the effectiveness of this algorithm in the multicolor superresolution imaging of bovine pulmonary arterial endothelial cells in our developed projection-based SIM system, which applies a computer controlled digital micromirror device for fast fringe generation and multicolor light-emitting diodes for illumination. The merit of the system incorporated with the proposed algorithm allows for a low excitation intensity fluorescence imaging even less than 1 W/cm², which is beneficial for the long-term, *in vivo* superresolved imaging of live cells and tissues.

© The Authors. Published by SPIE under a Creative Commons Attribution 3.0 Unported License. Distribution or reproduction of this work in whole or in part requires full attribution of the original publication, including its DOI. [DOI: [10.1117/1.JBO.21.9.096009](https://doi.org/10.1117/1.JBO.21.9.096009)]

Keywords: fluorescence; structured illumination; superresolution.

Paper 160144RRR received Mar. 7, 2016; accepted for publication Aug. 26, 2016; published online Sep. 20, 2016.

1 Introduction

In the past decades, fluorescence microscopy has evolved toward superresolution imaging.^{1–7} Structured illumination microscopy (SIM),^{8–11} as one of the most promising superresolution techniques, possesses the merits of a high framing rate and low excitation intensity, compared to the stimulated emission depletion microscopy (~800 MW/cm²),¹² the reversible saturable optical fluorescence transition microscopy (~1.7 MW/cm²),¹³ and the saturated SIM (~8 MW/cm²).¹⁴ SIM in its linear form can increase the imaging resolution by a factor of two beyond the traditional wide-field microscopy when illuminating through the imaging objective lens. In this approach, a periodic sinusoidal fringe illumination with a spatial frequency close to the diffraction limit is adopted to shift the unresolved high-frequency features of the sample to the optical transfer function (OTF) domain of the objective lens. In addition, speckle-based SIM,^{15,16} instant SIM,^{11,17} and other forms of SIM¹⁸ are presently gaining increasing interest. These techniques further enrich the theory and address parts of the limitations of traditional SIM. Nevertheless, the maximum resolution extension of SIM is only twofold over the conventional microscopy. Further improvement of resolution can be realized by utilizing the nonlinear response of fluorescence

molecules, such as saturated excitation (SE)^{14,19} or a photo-switchable (PS)^{20,21} mechanism. In practice, the SE-based nonlinear SIM requires high excitation intensity to satisfy the saturation condition that may harm the biological activity of living samples. For the PS-based nonlinear SIM, a relatively low intensity is permitted to activate the PS effect, but the photostability requirement for fluorescent dyes dramatically increases. Recently, the PS fluorescent protein was used in the PS-based nonlinear SIM technique developed by Betzig et al. to achieve 45- to 62-nm resolution.²¹ As the nonlinear SIM demands high excitation intensity or special fluorescent dyes with much more raw images required than the linear SIM, they also used a 1.7-NA objective to achieve 84-nm resolution under the linear total internal reflection fluorescence (TIRF)-SIM mode. Due to the advantages of low excitation power and high imaging speed, the linear SIM is still an ideal choice for dynamic imaging of living cells.

The generation and rapid phase control of high-quality fringe patterns is the key requirement in hardware for the SIM technique. This can be done by employing spatial light modulators (SLM), such as liquid crystal on silicon SLM, to generate adjustable orientation fringes by interference of two beams diffracted from the phase gratings addressed on the SLM.²² However, for maximal interference contrast, additional polarization control to maintain s-polarization for different fringe orientations is technically demanded, which often makes the optical configuration more complex. In addition, the high coherence of a laser beam inevitably produces speckle noises, which will seriously

*Address all correspondence to: Ming Lei, E-mail: leiming@opt.ac.cn; Baoli Yao, E-mail: yaobl@opt.ac.cn

degrade the image quality. Although dynamic averaging of the speckle noise using a rotating diffuser or random wagging of the homogenizers such as a multimode fibers phase modulator will produce a smooth image, it will also limit the image acquisition speed and increase the complexity of the system. To address these limitations, we previously developed a micromirror device (DMD)-based light-emitting diode (LED)-illumination SIM system.^{23,24} In that approach, a binary fringe pattern loaded on DMD is demagnified and projected onto the specimen. The higher orders of spatial frequencies of the binary fringe are naturally blocked off due to the low-pass filtering effect of the objective lens, leading to a sinusoidal fringe illumination in the sample plane. The DMD projection and LED-illumination system have a few advantages, including no polarization control, high throughput, ease of multiwavelength switching, and free of speckle-noise. However, it should be noticed that the modulation depth of the sinusoidal fringe illumination projected on the specimen is determined by the OTF of the objective, which makes it decrease with the increase of the fringe frequency and the imaging depth. The low modulation depth of patterns will affect the quality of the final reconstructed images. So, the image reconstruction algorithm is an important issue for high-quality superresolution image retrieval. In this process, it is crucial to precisely determine the parameters of the fringe illumination pattern, especially the initial phase estimation.²⁵ Incorrect initial phase estimation will seriously affect the superresolution result and leads to additional artifacts. Shroff et al.²⁶ have presented a method for estimating the pattern phase by analyzing the phase of peaks (POP) of the delta function in the spectral space of spatial frequency of the captured image. It is a commonly used algorithm in superresolution image reconstruction for the linear SIM.^{27,28} However, for high-frequency or low modulation depth illumination patterns, this algorithm is less reliable. Wicker et al.^{29,30} have proposed two alternative methods based on iterative cross-correlation and noniterative auto-correlation reconstruction (ACR) algorithms, respectively. These algorithms predominantly circumvent the limitation of the POP method in the condition of a high-frequency illumination pattern. Nevertheless, for a low modulation depth illumination pattern, they did not provide a detailed discussion. In short, although the DMD-projection-based LED-illumination SIM system successfully addresses parts of limitation arising from the liquid crystal spatial light modulator-based laser-illumination SIM system, the optimal reconstruction algorithm still remains a question especially at low modulation depth of illumination patterns to keep the fidelity of the superresolution image.

In this paper, we propose a reconstruction algorithm based on an image recombination transform (IRT) scheme to determine the initial phase accurately and simplify the process of extracting the high-order spectral components as well. The precise solution of the initial phase can be obtained without any approximate conditions even at a very low modulation depth of fringe illumination. The IRT algorithm does not contain an iterative operation, which makes the whole reconstruction process fast and automatic. The validity of the IRT algorithm is demonstrated by imaging the bovine pulmonary arterial endothelial (BPAE) cells in our built DMD-projection-based, multicolor-LED-illumination SIM system. The merit of the system incorporated with the proposed algorithm allows for fluorescence imaging at excitation intensity as low as 1 W/cm² using the LED light source, which represents a great decrease in excitation

intensity compared to existing SIM systems (e.g., 30 to 100 W/cm²).²¹ The IRT algorithm can also be applied for the laser interference-based SIM as a substitution of the POP algorithm.

2 Theoretical Analysis

Considering a specimen characterized by a spatial distribution of fluorophores density $S(r)$, it is illuminated by a cosine fringe intensity pattern $I(r)$ with the form

$$I(r) = I_0[1 + m \cdot \cos(2\pi p \cdot r + \varphi_0)], \quad (1)$$

where p and φ_0 are the spatial frequency and the initial phase of the cosine fringe pattern, I_0 and m are the mean intensity and modulation depth, respectively. In linear SIM, the in-focus portion $S_{\text{in}}(r)$ of the specimen is modulated by the structured illumination patterns $I(r)$ and the fluorescence emission intensity $E_{\text{in}}(r)$ is in linear response to the excitation light. Thus, we have

$$E_{\text{in}}(r) = I(r) \cdot S_{\text{in}}(r) = I_0[1 + m \cdot \cos(2\pi p \cdot r + \varphi_0)] \cdot S_{\text{in}}(r). \quad (2)$$

The captured fluorescence image by the detector can be described as a convolution of the emission fluorescence intensity and the point spread function (PSF) of the microscope. Thus, the in-focus image $D_{\text{in}}(r)$ formation is mathematically expressed as

$$D_{\text{in}}(r) = E_{\text{in}}(r) \otimes H(r) = \{I_0[1 + m \cdot \cos(2\pi p \cdot r + \varphi_0)] \cdot S_{\text{in}}(r)\} \otimes H(r), \quad (3)$$

where $H(r)$ represents the PSF of the microscope and the symbol \otimes denotes a convolution operation. Since the high spatial frequency excitation pattern attenuates very fast with defocus in the projection-type SIM, only the in-focus portion of the image is modulated, while the out-of-focus region is out of modulation.³¹ Therefore, the out-of-focus projection in the detected plane can be simplified as a nonmodulation item $B_{\text{out}}(r)$. Then, the final detected image can be rewritten as

$$D(r) = D_{\text{in}}(r) + B_{\text{out}}(r) = \{I_0[1 + m \cdot \cos(2\pi p \cdot r + \varphi_0)] \cdot S_{\text{in}}(r)\} \otimes H(r) + B_{\text{out}}(r). \quad (4)$$

In the frequency domain, the spectrum of the detected image can be obtained by making a Fourier transform to Eq. (4)

$$\begin{aligned} \tilde{D}(k) &= I_0[\tilde{S}_{\text{in}}(k) \otimes \delta(k) + \frac{m}{2} \tilde{S}_{\text{in}}(k) \\ &\quad \otimes \delta(k + p)e^{-i\varphi_0} + \frac{m}{2} \tilde{S}_{\text{in}}(k) \otimes \delta(k - p)e^{i\varphi_0}] \tilde{H}(k) \\ &\quad + \tilde{B}_{\text{out}}(k) \\ &= I_0[\tilde{S}_w(k) + \frac{m}{2} \cdot \tilde{S}_{\text{in}}(k + p)e^{-i\varphi_0} + \frac{m}{2} \\ &\quad \cdot \tilde{S}_{\text{in}}(k - p)e^{i\varphi_0}] \cdot \tilde{H}(k), \end{aligned} \quad (5)$$

with $\tilde{S}_w(k) = \frac{\tilde{S}_{\text{in}}(k) \cdot \tilde{H}(k) + \tilde{B}_{\text{out}}(k)}{\tilde{H}(k)}$.

The frequency distribution of $\tilde{S}_{\text{in}}(k + p)$ and $\tilde{S}_{\text{in}}(k - p)$ is the unresolvable high-frequency features of the sample and

shift to the support of the OTF, $\tilde{H}(k)$. Generally, in the reconstruction procedure of SIM, three raw images are taken with the fringe phase shifted by $2\pi/3$ between adjacent images. Combined with the deconvolution operation,^{32,33} the unresolved high-frequency features can be solved by Eq. (6) and only the frequency component $\tilde{S}_w(k)$ contains the out-of-focus information

$$\begin{bmatrix} \tilde{D}_1(k) \\ \tilde{D}_2(k) \\ \tilde{D}_3(k) \end{bmatrix} = I_0 H(k) \begin{bmatrix} 1 & \frac{m}{2} e^{-i\varphi_0} & \frac{m}{2} e^{i\varphi_0} \\ 1 & \frac{m}{2} e^{-i(\varphi_0+2\pi/3)} & \frac{m}{2} e^{i(\varphi_0+2\pi/3)} \\ 1 & \frac{m}{2} e^{-i(\varphi_0-2\pi/3)} & \frac{m}{2} e^{i(\varphi_0-2\pi/3)} \end{bmatrix} \times \begin{bmatrix} \tilde{S}_w(k) \\ \tilde{S}_{in}(k+p) \\ \tilde{S}_{in}(k-p) \end{bmatrix}. \quad (6)$$

To effectively extract the unresolved high-frequency information, the illumination pattern parameters of p , m , and φ_0 should be precisely determined, especially for the initial phase φ_0 , because it is included in the exponential term of the matrix. A small estimation error of φ_0 will result in a serious artifact in the reconstructed image.

Shroff et al.²⁶ have proposed the POP algorithm for estimating the initial phase, in which they analyze the value of the Fourier image at the pattern peak (i.e., $k = p$) with the form

$$\tilde{D}(p) = I_0 [\tilde{S}_w(p) + \frac{m}{2} \cdot \tilde{S}_{in}(2p) e^{-i\varphi_0} + \frac{m}{2} \cdot \tilde{S}_{in}(0) e^{i\varphi_0}] \cdot \tilde{H}(p). \quad (7)$$

It is noticed that when the out-of-focus background is weak, the frequency distribution of $\tilde{S}_w(k)$ is able to be approximated to the in-focus frequency distribution $\tilde{S}_{in}(k)$. If the power spectrum of the sample decreases sufficiently fast with growing frequency and also the modulation depth and the magnitude of OTF, $\tilde{H}(p)$, are sufficiently large, then the third term of Eq. (7) will be much larger than the remaining terms. In this case, we can ignore the small contribution of the first two terms in Eq. (7), and get the approximation of

$$\tilde{D}(p) \approx \frac{m}{2} \cdot I_0 \tilde{S}_{in}(0) \tilde{H}(p) \cdot e^{i\varphi_0}. \quad (8)$$

For any real valued samples and real PSF with symmetrical distribution, the center frequency component $\tilde{S}_{in}(0)$ and the OTF value $\tilde{H}(p)$ will be real. So, the phase contribution to Eq. (8) will only come from $e^{i\varphi_0}$. Hence, the initial phase can be estimated by solving the phase of this peak

$$\varphi_0 \approx \arg[\tilde{D}(p)]. \quad (9)$$

The POP algorithm works well when all the above assumptions are fulfilled. For example, in the TIRF-SIM where the fluorescence excitation is generated in a thin volume with a depth typically below 200 nm, this excitation scheme has a very weak background and the POP algorithm can provide good precision in estimating the initial phase and separating the components well. However, in some cases, such as an existing strong background, or having a weak modulation depth or high-frequency illumination pattern, the POP algorithm cannot give an appropriate result.^{29,30}

To address the limitation of the POP algorithm, here, we employ the phase shift between two adjacent images by $\pi/2$ rather than the commonly used value of $2\pi/3$. Using Eq. (4), we can easily obtain the expression of the three captured images

$$\begin{aligned} D_1(r) &= \{I_0[1 + m \cdot \cos(2\pi p \cdot r + \varphi_0)] \cdot S_{in}(r)\} \\ &\quad \otimes H(r) + B_{out}(r), \\ D_2(r) &= \{I_0[1 - m \cdot \sin(2\pi p \cdot r + \varphi_0)] \cdot S_{in}(r)\} \\ &\quad \otimes H(r) + B_{out}(r), \\ D_3(r) &= \{I_0[1 - m \cdot \cos(2\pi p \cdot r + \varphi_0)] \cdot S_{in}(r)\} \\ &\quad \otimes H(r) + B_{out}(r). \end{aligned} \quad (10)$$

Because the intensity of the out-of-focus background $B_{out}(r)$ remains a constant, we can subtract two adjacent phase-shifted raw images to eliminate the background contribution

$$\begin{aligned} D_{12}(r) &= D_1(r) - D_2(r) \\ &= \sqrt{2}m \cdot I_0 \cdot \left\{ \left[\cos(2\pi p \cdot r + \varphi_0) \cos \frac{\pi}{4} \right. \right. \\ &\quad \left. \left. + \sin(2\pi p \cdot r + \varphi_0) \sin \frac{\pi}{4} \right] \cdot S_{in}(r) \right\} \otimes H(r) \\ &= \sqrt{2}m \cdot I_0 [\cos(2\pi p \cdot r + \varphi_0 - \pi/4) \cdot S_{in}(r)] \otimes H(r), \end{aligned} \quad (11)$$

$$\begin{aligned} D_{23}(r) &= D_2(r) - D_3(r) \\ &= -\sqrt{2}m \cdot I_0 \cdot \left\{ \left[\sin(2\pi p \cdot r + \varphi_0) \cos \frac{\pi}{4} - \cos(2\pi p \cdot r \right. \right. \\ &\quad \left. \left. + \varphi_0) \sin \frac{\pi}{4} \right] \cdot S_{in}(r) \right\} \otimes H(r) \\ &= -\sqrt{2}m \cdot I_0 [\sin(2\pi p \cdot r + \varphi_0 - \pi/4) \cdot S_{in}(r)] \otimes H(r). \end{aligned} \quad (12)$$

Then, we recombine a complex image by setting $D_{12}(r)$ as the real part and $D_{23}(r)$ as the imaginary part, respectively,

$$\begin{aligned} D_c(r) &= D_{12}(r) - i \cdot D_{23}(r) \\ &= \sqrt{2} [m \cdot I_0 e^{i(2\pi p r + \varphi_0 - \pi/4)} \cdot S_{in}(r)] \otimes H(r). \end{aligned} \quad (13)$$

The Fourier transform of the recombined complex image is presented in the form

$$\tilde{D}_c(k) = \sqrt{2} m e^{i(\varphi_0 - \pi/4)} \cdot I_0 \tilde{S}_{in}(k - p) \cdot \tilde{H}(k). \quad (14)$$

Substituting $k = p$ into Eq. (14), we obtain

$$\tilde{D}_c(p) = A(p) \cdot e^{i(\varphi_0 - \pi/4)}, \quad (15)$$

where $A(p) = \sqrt{2}m \cdot I_0 \tilde{S}_{in}(0) \cdot \tilde{H}(p)$. As discussed above, $A(p)$ is real valued in the condition of real sample and symmetrical real PSF. Thus, the initial phase can be solved by

$$\varphi_0 = \arg[\tilde{D}_c(p)] + \pi/4. \quad (16)$$

It should be mentioned that if the noise is too high, the estimation will be disabled. After solving $\tilde{D}_c(p)$, one side of the

unresolved high-frequency component can then be simply extracted by Eq. (14)

$$\tilde{S}_{in}(k-p) = \frac{e^{i \arg\{\tilde{D}_c(p)\}} \cdot \tilde{D}_c(k)}{\sqrt{2mI_0}\tilde{H}(k)}. \quad (17)$$

Similarly, we can construct a conjugate image of the complex image $D_c(r)$. Then, the other side of the unresolved high-frequency component can also be extracted in the following expression:

$$\tilde{S}_{in}(k+p) = \frac{e^{i \arg\{\tilde{D}_{cc}(-p)\}} \cdot \tilde{D}_{cc}(k)}{\sqrt{2mI_0}\tilde{H}(k)}, \quad (18)$$

where $\tilde{D}_{cc}(k) = \text{FT}\{D_c^*(r)\}$, $\arg\{\tilde{D}_c(p)\} = -\arg\{\tilde{D}_{cc}(-p)\} - \pi/2$, FT and the symbol * denote the Fourier transform and the conjugation operation, respectively. Also, the wide-field component is easy to acquire by the Fourier transform of the sum of $D_1(r)$ and $D_3(r)$. In summary, the IRT algorithm first determines the initial phase by Eq. (16) and then subsequently retrieves the unresolved high-frequency components by Eqs. (17) and (18). After shifting the components to the correct positions and making deconvolution with the generalized Wiener filter, the final extended spectrum can be obtained, and then by taking an inverse Fourier transform, the super-resolved image can be reconstructed.

Compared to the POP algorithm described by Eq. (9), the proposed IRT algorithm can provide a precise solution of the fringe initial phase without the assumptions of weak background and high modulation depth. In addition, the IRT algorithm can directly solve the unresolved in-focus high-frequency components of $\tilde{S}_{in}(k+p)$ and $\tilde{S}_{in}(k-p)$ by Eqs. (17) and (18), avoiding having to solve the matrix equation of Eq. (6).

3 Numerical Simulation

To verify the validity and feasibility of the IRT method, we first make a numerical simulation. In the simulation, the fringe illumination pattern is projected onto the sample through an oil-immersed objective (100 \times , NA = 1.49, $n = 1.515$). The fluorescence signal (emission wavelength at 461 nm) is collected by a digital camera (2048 \times 2048 pixels, pixel size 6.5 $\mu\text{m} \times 6.5 \mu\text{m}$). The virtual object and its Fourier transform spectrum are shown in Figs. 1(a) and 1(b), respectively.

According to the Abbe's diffraction limit equation, the minimum period of the projection fringe is 155 nm at $\lambda = 461$ nm with objective of NA = 1.49. The initial phase estimation error under the condition of low modulation depth ranging from 0.001 to 0.12 with the fringe period of 193 and 156 nm are calculated by the POP, ACR, and IRT algorithms, respectively, as shown in Fig. 2. In theory, the phase error of the IRT algorithm should be zero in the absence of noise. The phase errors of the POP and ACR algorithms increase rapidly when the modulation depth is below 0.04 and 0.02, respectively, even without noise contribution, while the IRT algorithm always retains a relatively high precision over the whole range of the modulation depth. Considering Poisson noise is the predominant type of noise in low intensity images, we first add the Poisson noise in simulation [Figs. 2(a) and 2(c)] for comparing the performance of different algorithms. In this case, the maximal phase errors of the POP, ACR, and IRT algorithms read 7.9 deg, 7.3 deg, and 0.2 deg, respectively, at the period of 193 nm, corresponding to 80% of the maximum frequency supported by the OTF. When the fringe period decreases to 156 nm, approximating to the diffraction limit of the simulated system, the maximal phase errors of the POP algorithm increases up to 61 deg at the modulation depth of 0.001. On the other hand, the major contribution of electronic noise is mostly the Gaussian distribution. Thus, the comparison for the phase errors with Gaussian noise is also simulated in Fig. 2. The variances of the noise distribution are set to 0.001 [Figs. 2(b) and 2(d)]. Note that the sample spectrum signal is so weak at the OTF edge that the Gaussian noise becomes a major contribution. Therefore, the error curves fluctuate strenuously with the fringe period decreasing in the presence of Gaussian noise. In that condition, the IRT algorithm still can provide a relatively acceptable result, especially at the fringe period of 193 nm.

In short, for raw images with high modulation depth, all the algorithms are able to give a good performance in reducing the phase error. But in the condition of low modulation depth, only the IRT algorithm can estimate the initial phase with the best precision. However, similar to the other algorithms, if the noise is too strong, the IRT algorithm may not guarantee an acceptable precision of the initial phase.

To make a superresolution image reconstruction of SIM, three orientations of illumination fringes at 0 deg, 60 deg, and 120 deg are performed at the fringe period of 156 nm. The reconstructed images of the simulated object are shown

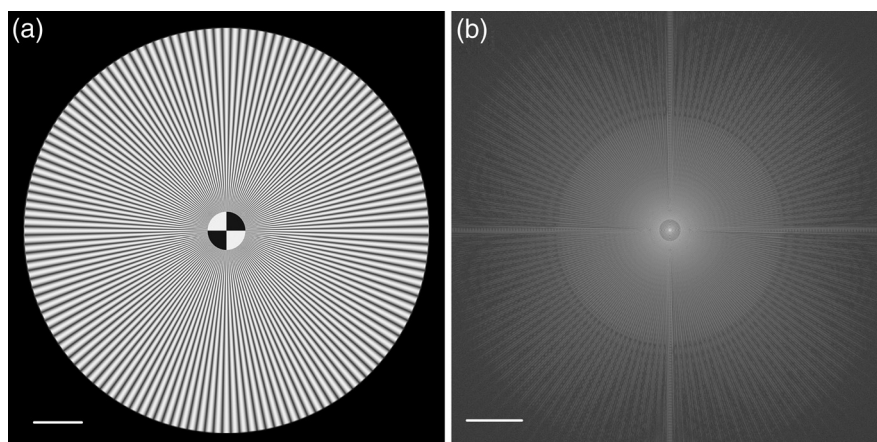


Fig. 1 (a) Virtual object and (b) its Fourier transform spectrum. Scale bar: (a) 5 μm and (b) 2 μm^{-1} .

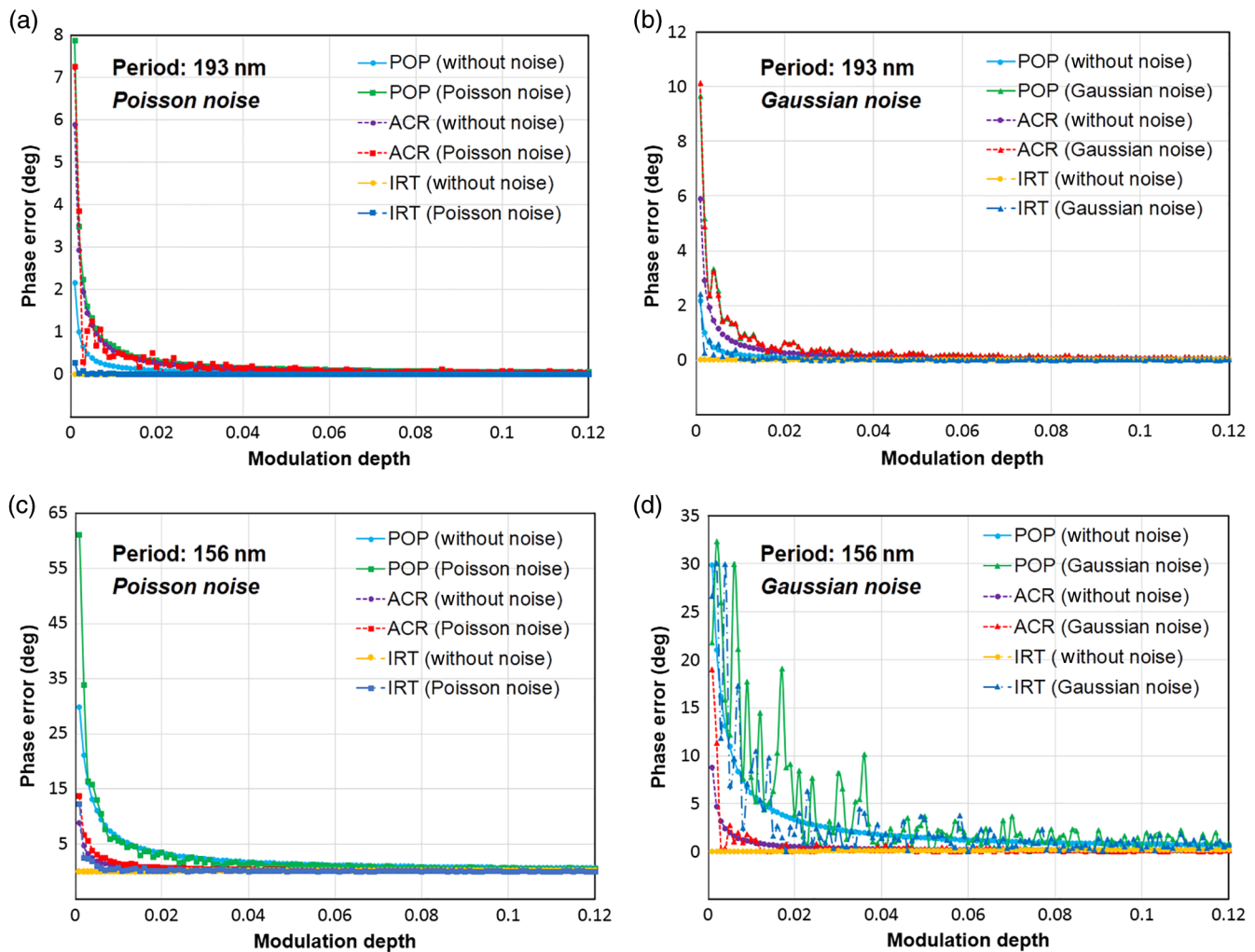


Fig. 2 Simulation of initial phase estimation error under low modulation depth of illumination fringe at the period of (a) and (b) 193 nm and (c) and (d) 156 nm. For analyzing the influence of noises, the simulated images are degraded with (a) and (c) Poisson noise and (b) and (d) Gaussian noise with the variance of 0.001, respectively. In the presence of weak noises, the IRT algorithm exhibits excellent performance for low modulation depth.

in Fig. 3 with different algorithms at different modulation depth of fringe for comparison. Figure 3(a) is the wide-field image and its central region marked by a dashed box is magnified. Figures 3(b)–3(d) are the corresponding magnified super-resolution images reconstructed by the IRT algorithm, Figs. 3(e)–3(g) and 3(h)–3(j) are corresponding to the ACR algorithm and the POP algorithm. The Fourier spectra of each reconstructed image are displayed at the top-right corners of the magnified images. It can be seen that all of the algorithms can successfully extend the support of the OTF in the frequency domain and enhance the spatial resolution of the image. However, with the decrease of the modulation depth, it is more and more difficult for the POP algorithm to separate the components well, and thus some residual errors come into being because of the estimation error of the initial phase. As previously speculated, owing to the incorrect spectrum expansion, a series of wave-like artifacts appear in the reconstructed images. This is particularly evident in Fig. 3(h). On the other hand, although the ACR algorithm is an effective method for phase estimation, the reconstruction process is time-consuming compared to the POP and IRT algorithms. Meanwhile, when the modulation

depth is less than 0.01, a slight wave-like artifact also appears in the reconstructed image. In contrast, the IRT algorithm always retains a good performance even under low modulation depth, as seen in Fig. 3(b). When the modulation depth increases to more than 0.1, all of the algorithms give the same results.

4 Experiments and Results

To further prove the applicability of the IRT algorithm, we used our developed DMD-projection-based LED-illumination SIM system^{23,24} to carry out the following experiment. The scheme of the SIM system is shown in Fig. 4. A four-wavelength high-power LEDs assembly (LED4D251, Thorlabs Inc.) with switchable wavelengths of 405, 470, 565, and 625 nm is employed as the illumination source for multiwavelength excitation. The LED light enters the TIR-Prism and is reflected to the DMD chip (DLP7000UV, Texas Instruments Inc.), where the fringe pattern is loaded. The light modulated by the DMD passes through a demagnifying optical system, consisting of a collimating lens, and a 100× objective (Apo TIRF, NA1.49, Nikon Inc., Japan), to produce a sinusoidal fringe illumination projected

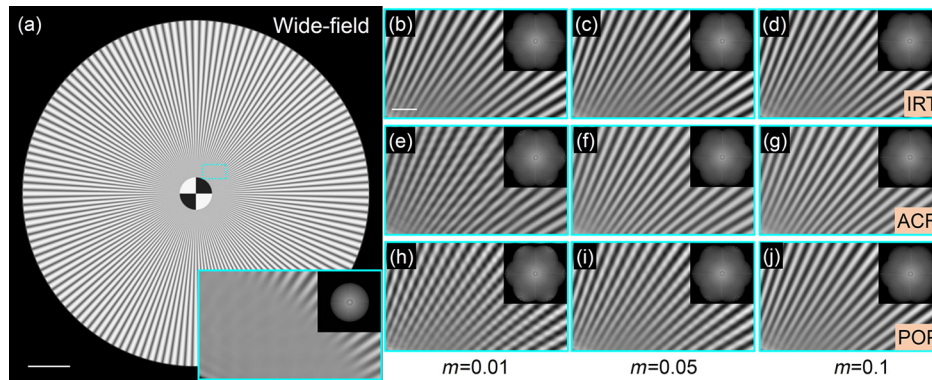


Fig. 3 Reconstructed images of the simulated object using different methods at different modulation depth of fringe illumination. (a) The wide-field image and its magnified central part of the dashed boxed region. (b)–(g) The corresponding magnified superresolution images reconstructed by the IRT algorithm (b)–(d), the ACR algorithm (e)–(g) and the POP algorithm (h)–(j) at different modulation depth for comparison of the reconstructed image quality. The Fourier spectra of each reconstructed image are illustrated at the top-right corners, respectively. Compared to the wide-field image, all of the reconstruction methods are able to enhance the spatial resolution. However, with the decrease of the modulation depth, the reconstructed image by the POP algorithm produces more artifacts, while the IRT algorithm always retains a satisfactory performance. Scale bar: (a) $5\ \mu\text{m}$ and (b)–(g) $500\ \text{nm}$.

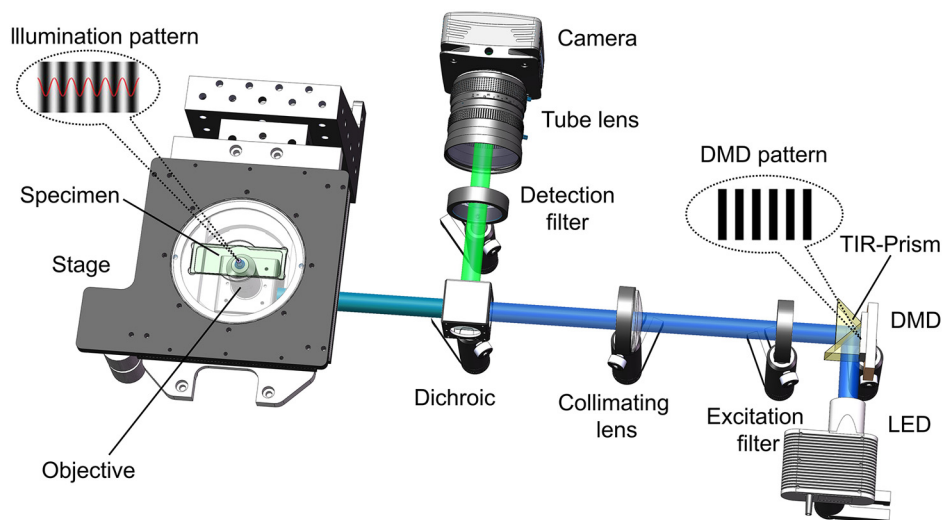


Fig. 4 Schematic of the DMD-projection-based LED-illumination SIM system. LED: multiwavelengths of $405\ \text{nm}/470\ \text{nm}/565\ \text{nm}/625\ \text{nm}$; DMD: maximal binary pattern rate of $32\ \text{kHz}$ at 1024×768 pixels with a pixel pitch of $13.68\ \mu\text{m}$; excitation filter: quad-band bandpass of $390 \pm 22\ \text{nm}/482 \pm 11\ \text{nm}/563 \pm 7\ \text{nm}/640 \pm 10\ \text{nm}$; dichroic: quad-edge reflection bands of 370 to $410\ \text{nm}/473$ to $491\ \text{nm}/559$ to $568\ \text{nm}/633$ to $647\ \text{nm}$; detection filter: quad-band bandpass of $446 \pm 18\ \text{nm}/523 \pm 23\ \text{nm}/600 \pm 20\ \text{nm}/677 \pm 17\ \text{nm}$; objective: $100 \times / \text{NA}\ 1.49$; camera: maximum frame rate of $100\ \text{fps}$ at 2048×2048 pixels with a pixel pitch of $6.5\ \mu\text{m}$.

onto the specimen. A quad-band filter set (including a $390/482/563/640\ \text{nm}$ quad-band bandpass excitation filter, a $446/523/600/677\ \text{nm}$ quad-band bandpass emission filter, and a $R405/488/561/635\ \text{nm}$ quad-edge dichroic beamsplitter, Semrock Inc.) are used to separate the excitation lights and the emission fluorescence signals. A sCMOS camera with a maximum full-frame rate of $100\ \text{fps}$ (Orca Flash4.0, 2048×2048 pixels, 16 bits gray depth, Hamamatsu Inc., Japan) is used to capture the two-dimensional image. The phase shifts of the fringe are controlled by the DMD chip without mechanical movement. If the fringe period is designed to occupy N pixels on the DMD chip, the minimum value of the phase shift will be

$2\pi/N$. Thus, to achieve a $\pi/2$ phase shift, just setting four pixels per period on the DMD chip, the illumination fringe phases corresponding to φ_0 , $\varphi_0 + \pi/2$, and $\varphi_0 + \pi$, will be obtained, respectively. In order to achieve a high imaging speed and a simplified pattern design, we apply only two perpendicular illumination fringe orientations in the experiment. Nevertheless, it is possible to generate multiorientation illuminations with specifically designed illumination patterns.

The photobleaching and phototoxicity effects have constantly been obstacles to long-term observation of living cells in fluorescence microscopy. The high excitation intensity will accelerate the photobleaching of fluorescent molecules and

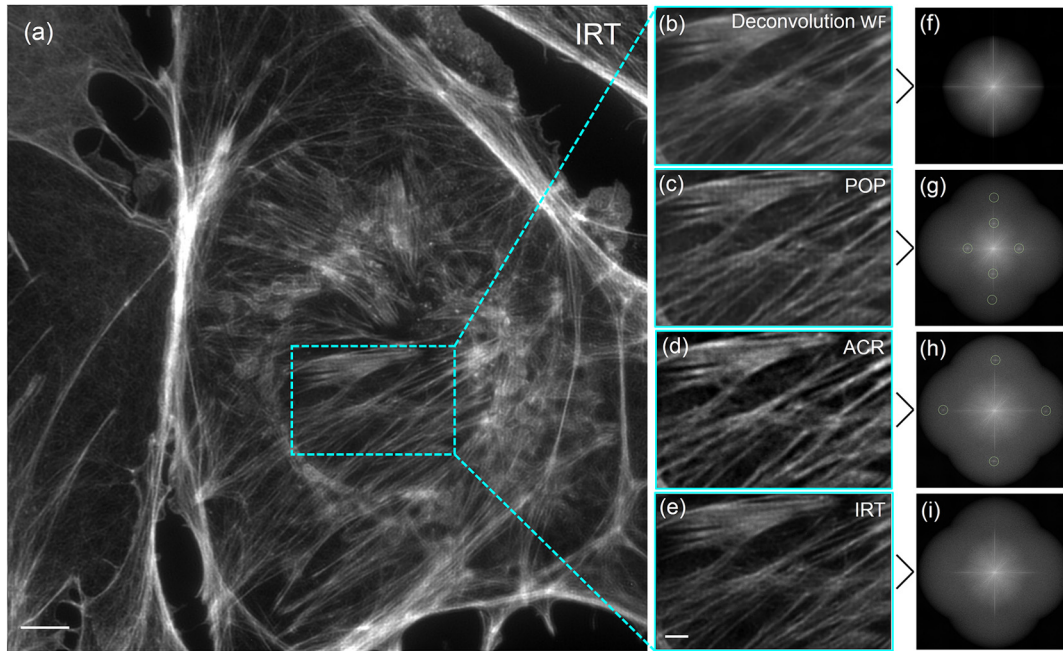


Fig. 5 (a) The reconstructed superresolution image of F-actin in BPAE cells without artifacts by the IRT algorithm. For comparison, the magnified views of the dash-boxed region in (a) by different methods are, respectively, shown in (b)–(e), and the corresponding Fourier spectra are shown in (f)–(i). Some of residual components [indicated by pale-green circles in (g) and (h)] appear in the Fourier spectrum with the ACR algorithm and the POP algorithm, resulting in some unwanted information in the reconstructed image (c) and (d). In contrast, the IRT algorithm separates the components well in the Fourier spectrum (i), and thus effectively avoid artifacts and obtain a clear image (e). Scale bar: (a) 3 μm and (b)–(e) 1 μm .

be harmful to specimens.³⁴ The excitation intensities for the existing SIM systems (e.g., 30 to 100 W/cm^2) are usually much stronger than that of the wide-field or light-sheet microscopies. In this experiment, we could image at intensities as low as 1 W/cm^2 , which is close to the life evolved condition

(0.1 W/cm^2).³⁵ This makes the system more suitable for bio-imaging of low excitation intensities and long-term observation of specimens.

To demonstrate the feasibility of the IRT algorithm for the projection-based SIM, we employ the trichrome-stained BPAE

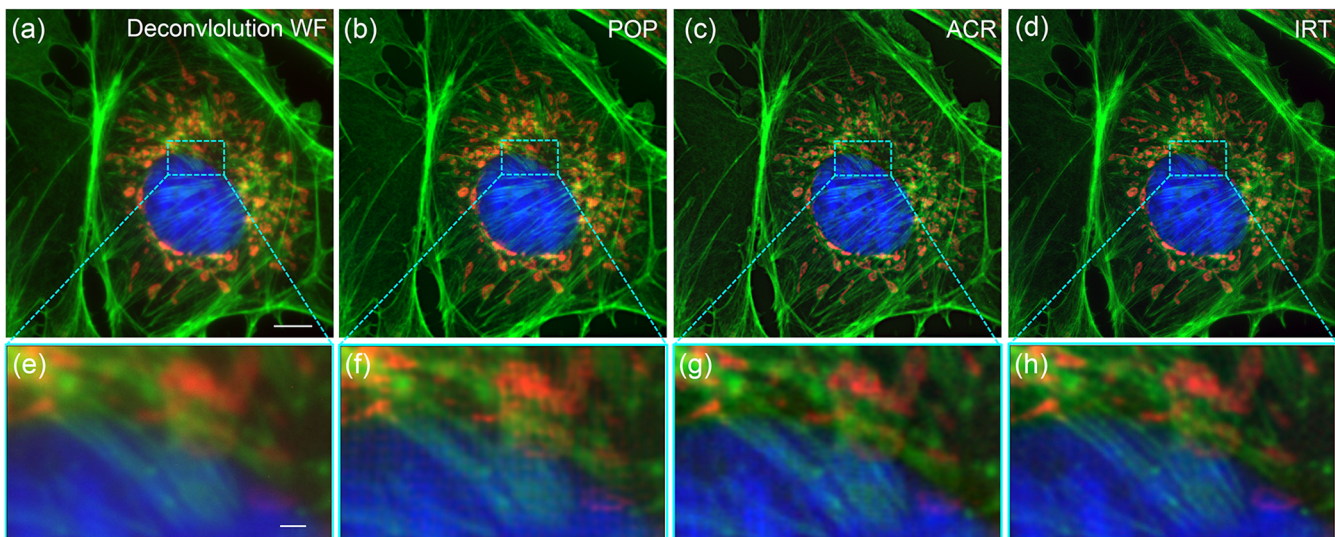


Fig. 6 Superimposed images of the trichrome-stained BPAE cells reconstructed by different methods. (a) Deconvolution wide-field image, (b) superresolution image reconstructed by the POP algorithm, (c) superresolution image reconstructed by the ACR algorithm, (d) superresolution image reconstructed by the IRT algorithm. (e)–(h) The magnified views of the dash-boxed regions, respectively. Mitochondria are rendered in red, F-actins are rendered in green and nuclei are rendered in blue. Scale bar: (a)–(d) 5 μm and (e)–(h) 500 nm.

cells (F36924, Thermo Fisher Scientific Inc.) as the specimen, which are labeled with MitoTracker Red CMXRos for Mitochondria, Alexa Fluor 488 phalloidin for F-actin, and DAPI for nuclei. The cells are sequentially illuminated using the excitation wavelengths of 405, 470, and 565 nm to achieve multicolor images. In this experiment, the modulation depth of the fringe is measured to be 0.046. Figure 5(a) shows a high-fidelity superresolution image of the F-actin obtained by the IRT algorithm. By applying the POP algorithm to process the same raw data, some unwanted residues appear in the Fourier spectrum as indicated by the pale-green circles in Fig. 5(g), resulting in some artifacts in the reconstructed image of Fig. 5(c). Compared to the POP algorithm, the ACR algorithm obtains an improvement in artifacts suppression and the residual fringes are hardly seen in its reconstructed image [Fig. 5(d)]. But there still exist a few extra components in the Fourier spectrum [Fig. 5(h)], leading to the reduction of image quality. In terms of computation time, the POP, ACR, and IRT algorithms take 2.97, 9.65, and 3.02 s, respectively, to calculate one superresolution image from six raw images (2048×2048 pixels) using a personal computer (Intel Core i7-4790K 4 GHz processor and 32 GB RAM) with the MATLAB software (R2013a) operating under Windows 7 (SP1) x64. Similar experimental results of superimposed tricolor images of BPAE cells are shown in Fig. 6. Here, the mitochondria are rendered in red, the F-actins are rendered in green, and the nuclei are rendered in blue. By the POP algorithm, the F-actin and mitochondria exhibit some extra stripes in the reconstructed images [Figs. 6(b) and 6(f)]. These artifacts may confuse the scientific evaluation of biological morphology. However, in the IRT superresolution images [Figs. 6(d) and 6(h)], such residual stripes are not observed and the image qualities are better than the ACR images shown in Figs. 6(c) and 6(g). This once again proves that the IRT algorithm is a robust and high-accuracy reconstruction method for superresolution imaging.

Although the IRT algorithm is immune to the modulation depth of the illumination fringe, it should be noticed that the noise in the captured structured illumination images is another challenge to the accurate determination of the initial phase. In fact, when the image noise is too high, Eq. (15) cannot be strictly tenable, because the noise contribution must be considered. As a result, the solution of the initial phase of Eq. (16) will contain a phase error. So, obtaining a high signal-to-noise ratio (SNR) of structured illumination images is crucial for increasing the accuracy of initial phase determination. In our system, we use a high sensitivity sCMOS camera with 16 bits gray depth to capture high SNR images, which guarantees obtaining high-fidelity superresolution images. Based on the potential advantages of the DMD-projection-based LED-illumination SIM system, incorporated with the proposed IRT superresolution algorithm, future work will be extended to fast multicolor live-cell imaging and object tracking.

5 Conclusion

We have proposed an IRT superresolution image reconstruction algorithm for SIM. Compared to the traditional POP algorithm and the ACR algorithm, the IRT algorithm can obtain the initial phase of fringe with high precision, and extract the high-order spectral components without matrix operation. Numerical simulations show that the IRT algorithm always keeps a higher precision of initial phase estimation than the POP algorithm. The immunity of the IRT algorithm against the modulation depth of fringe patterns and the high precision of initial phase

determination enable reconstructing an artifact-free superresolution image as long as the SNR of the captured images is reasonably high. We have proved the feasibility and reliability of the IRT algorithm by employing it in our built DMD-projection-based, multicolor-LED-illumination SIM system to image the BPAE cells at low excitation intensity. The experimental results demonstrate that the IRT method can effectively avoid artifacts to produce high-fidelity superresolution images. The IRT algorithm is applicable in either the projection-based SIM or the interference-based SIM.

Acknowledgments

This research was supported by the Natural Science Foundation of China (NSFC) under Grant Nos. 61522511, 11404389, 81427802, and 61275193.

References

1. S. W. Hell and J. Wichmann, "Breaking the diffraction resolution limit by stimulated emission: stimulated-emission-depletion fluorescence microscopy," *Opt. Lett.* **19**(11), 780–782 (1994).
2. M. Hofmann et al., "Breaking the diffraction barrier in fluorescence microscopy at low light intensities by using reversibly photoswitchable proteins," *Proc. Natl. Acad. Sci. U. S. A.* **102**(49), 17565–17569 (2005).
3. E. Betzig et al., "Imaging intracellular fluorescent proteins at nanometer resolution," *Science* **313**(5793), 1642–1645 (2006).
4. S. T. Hess, T. P. Girirajan, and M. D. Mason, "Ultra-high resolution imaging by fluorescence photoactivation localization microscopy," *Biophys. J.* **91**(11), 4258–4272 (2006).
5. M. J. Rust, M. Bates, and X. Zhuang, "Sub-diffraction-limit imaging by stochastic optical reconstruction microscopy (STORM)," *Nat. Methods* **3**(10), 793–796 (2006).
6. J. Fölling et al., "Fluorescence nanoscopy by ground-state depletion and single-molecule return," *Nat. Methods* **5**(11), 943–945 (2008).
7. M. Heilemann et al., "Subdiffraction-resolution fluorescence imaging with conventional fluorescent probes," *Angew. Chem. Int. Ed.* **47**(33), 6172–6176 (2008).
8. R. Heintzmann and C. G. Cremer, "Laterally modulated excitation microscopy: improvement of resolution by using a diffraction grating," *Proc. SPIE* **3568**, 185–196 (1999).
9. M. G. Gustafsson, "Surpassing the lateral resolution limit by a factor of two using structured illumination microscopy," *J. Microsc.* **198**(2), 82–87 (2000).
10. A. G. York et al., "Resolution doubling in live, multicellular organisms via multifocal structured illumination microscopy," *Nat. Methods* **9**(7), 749–754 (2012).
11. A. G. York et al., "Instant super-resolution imaging in live cells and embryos via analog image processing," *Nat. Methods* **10**(11), 1122–1126 (2013).
12. B. Hein, K. I. Willig, and S. W. Hell, "Stimulated emission depletion (STED) nanoscopy of a fluorescent protein-labeled organelle inside a living cell," *Proc. Natl. Acad. Sci. U. S. A.* **105**(38), 14271–14276 (2008).
13. T. Grotjohann et al., "rsEGFP2 enables fast RESOLFT nanoscopy of living cells," *Elife* **1**, e00248 (2012).
14. M. G. Gustafsson, "Nonlinear structured-illumination microscopy: wide-field fluorescence imaging with theoretically unlimited resolution," *Proc. Natl. Acad. Sci. U. S. A.* **102**(37), 13081–13086 (2005).
15. E. Mudry et al., "Structured illumination microscopy using unknown speckle patterns," *Nat. Photonics* **6**(5), 312–315 (2012).
16. A. Negash et al., "Improving the axial and lateral resolution of three-dimensional fluorescence microscopy using random speckle illuminations," *J. Opt. Soc. Am. A* **33**(6), 1089–1094 (2016).
17. P. W. Winter et al., "Two-photon instant structured illumination microscopy improves the depth penetration of super-resolution imaging in thick scattering samples," *Optica* **1**(3), 181–191 (2014).
18. M. Schropp and R. Uhl, "Two-dimensional structured illumination microscopy," *J. Microsc.* **256**(1), 23–36 (2014).
19. R. Heintzmann, "Saturated patterned excitation microscopy with two-dimensional excitation patterns," *Micron* **34**(6), 283–291 (2003).

20. E. H. Rego et al., "Nonlinear structured-illumination microscopy with a photoswitchable protein reveals cellular structures at 50-nm resolution," *Proc. Natl. Acad. Sci. U. S. A.* **109**(3), E135–E143 (2012).
21. D. Li et al., "Extended-resolution structured illumination imaging of endocytic and cytoskeletal dynamics," *Science* **349**(6251), aab3500 (2015).
22. R. Fiolka et al., "Time-lapse two-color 3D imaging of live cells with doubled resolution using structured illumination," *Proc. Natl. Acad. Sci. U. S. A.* **109**(14), 5311–5315 (2012).
23. D. Dan et al., "DMD-based LED-illumination super-resolution and optical sectioning microscopy," *Sci. Rep.* **3**, 1116 (2013).
24. J. Qian et al., "Full-color structured illumination optical sectioning microscopy," *Sci. Rep.* **5**, 14513 (2015).
25. L. Schaefer, D. Schuster, and J. Schaffer, "Structured illumination microscopy: artefact analysis and reduction utilizing a parameter optimization approach," *J. Microsc.* **216**(2), 165–174 (2004).
26. S. A. Shroff, J. R. Fienup, and D. R. Williams, "Phase-shift estimation in sinusoidally illuminated images for lateral superresolution," *J. Opt. Soc. Am. A* **26**(2), 413–424 (2009).
27. S. Chowdhury, A.-H. Dhalla, and J. Izatt, "Structured oblique illumination microscopy for enhanced resolution imaging of non-fluorescent, coherently scattering samples," *Biomed. Opt. Express* **3**(8), 1841–1854 (2012).
28. R. W. Lu et al., "Super-resolution scanning laser microscopy through virtually structured detection," *Biomed. Opt. Express* **4**(9), 1673–1682 (2013).
29. K. Wicker et al., "Phase optimisation for structured illumination microscopy," *Opt. Express* **21**(2), 2032–2049 (2013).
30. K. Wicker, "Non-iterative determination of pattern phase in structured illumination microscopy using auto-correlations in Fourier space," *Opt. Express* **21**(21), 24692–24701 (2013).
31. S. Monneret, M. Rauzi, and P. Lenne, "Highly flexible whole-field sectioning microscope with liquid-crystal light modulator," *J. Opt. A: Pure Appl. Opt.* **8**(7), S461 (2006).
32. M. G. Gustafsson et al., "Three-dimensional resolution doubling in wide-field fluorescence microscopy by structured illumination," *Biophys. J.* **94**(12), 4957–4970 (2008).
33. B. Thomas, M. Momany, and P. Kner, "Optical sectioning structured illumination microscopy with enhanced sensitivity," *J. Opt.* **15**(9), 094004 (2013).
34. G. H. Patterson and D. W. Piston, "Photobleaching in two-photon excitation microscopy," *Biophys. J.* **78**(4), 2159–2162 (2000).
35. E. H. Stelzer, "Light-sheet fluorescence microscopy for quantitative biology," *Nat. Methods* **12**(1), 23–26 (2015).

Xing Zhou is a PhD candidate at Xi'an Institute of Optics and Precision Mechanics, Chinese Academy of Sciences, and a jointly educated PhD candidate at School of Science, Xi'an Jiaotong University. He received his BS degree in physics at Nankai University in 2012. His research focuses on the super-resolution optical microscopy and optical sectioning imaging, especially the structured illumination microscopy and light sheet microscopy.

Ming Lei is a professor at Xi'an Institute of Optics and Precision Mechanics, Chinese Academy of Sciences. He received his PhD

degree at Xi'an Institute of Optics and Precision Mechanics, Chinese Academy of Sciences in 2007, and the BE degree at the School of Physics and Optoelectronic Engineering, Xidian University, in 2000. He has published more than 80 papers and holds 9 Chinese patents. His current research focuses on super-resolution microscopy and optical trapping technologies.

Dan Dan is an assistant professor and a PhD candidate at Xi'an Institute of Optics and Precision Mechanics, Chinese Academy of Sciences. He received his MS degree in physical electronics at the School of Physics and Optoelectronic Engineering, Xidian University, in 2010. His current research focuses on structured illumination microscopy for super-resolution and optical sectioning.

Baoli Yao is a professor at Xi'an Institute of Optics and Precision Mechanics, Chinese Academy of Sciences. He received his PhD degree at Xi'an Institute of Optics and Precision Mechanics, Chinese Academy of Sciences, in 1997. His research areas include super-resolution microscopy, digital holographic microscopy, optical micro-manipulation, optical data storage, and special optical beams. He has published more than 180 papers in peer-reviewed journals and three book chapters, and owned sixteen authorized Chinese invention patents.

Yanlong Yang is a senior engineer and a PhD candidate at Xi'an Institute of Optics and Precision Mechanics, Chinese Academy of Sciences. He received his MS degree in applied physics at Xi'an Jiaotong University in 2001. His research is focused on the development of two-photon excitation laser scanning fluorescence stereomicroscopy.

Jia Qian is a PhD candidate at Xi'an Institute of Optics and Precision Mechanics, Chinese Academy of Sciences. He received his BS degree at the School of Physics and Optoelectronic Engineering, Xidian University, in 2012. His research topic is the full-color structured illumination optical sectioning microscopy with large field of view and high resolution.

Guangde Chen is a professor at School of Science, Xi'an Jiaotong University. He received his MS degree in optics in the Department of Physics, Xi'an Jiaotong University, in 1989. His research focuses on investigating the mechanisms of optical transitions and lasing in nitride materials to understand the fundamental optical transitions and dynamic processes and to study the physics components of optoelectronic devices.

Piero R. Bianco is an associate professor at the Department of Microbiology and Immunology, University at Buffalo, United States. He received his BS degree in biology at Abilene Christian University in 1987, and the PhD degree in biochemistry at University of Texas Medical School at Houston in 1993. He pursued postdoctoral work in physical biochemistry and biophysics, UC Davis. His research activity is focused on the genetic recombination and DNA repair and single molecule studies.